

# Highly hydrothermally stable Al-MCM-41 with accessible void defects

Zhanquan Zhang · Zifeng Yan

Published online: 4 June 2012  
© Springer Science+Business Media, LLC 2012

**Abstract** Mesoporous aluminosilicates (Al-MCM-41) with high hydrothermal stability were synthesized via self-assembly of nanoseed precursors, obtained from alkali-treatment of ZSM-5. Characterized by N<sub>2</sub> sorption, Transmission electron microscopy, Fourier transform infrared spectroscopy, X-ray diffraction, and Mercury intrusion, as-prepared Al-MCM-41 possessed a large number of void defects, enhancing the connectivity of MCM-41. The effects of alkali-treatment degree, including time and concentration, on volume of void defects were investigated and discussed. It is revealed that volume of void defects decreased in the severe condition of alkali-treatment, and void defects representing the intraparticular pores account for a volume of 0.138 cm<sup>3</sup>/g in Al-MCM-41, prepared under the condition of 1.0 mol/L of NaOH and 1 h of stirring time. A tentative proposed mechanism for interpreting the formation of void defects was presented. Aggregated secondary building units in the precursors not only provided Si (Al) sources, but also functioned as templates for the development of void defects. Al-MCM-41 with void defects would be beneficial to diffusion and mass transportation.

**Keywords** Void defects · Hysteresis loop · Aggregated structure · MCM-41

## 1 Introduction

Ordered mesoporous aluminosilicates have attracted more attention and interests due to their unique properties (e.g., high surface area, ordered mesopores) and increasing demands of petrochemical field since the upsurge of M41S family [1, 2]. It was soon realized that the behavior of conventional mesoporous materials in acidic catalytic reactions and harsh vapor conditions, fell short of expectation due to the lack of acid strength and hydrothermal stability [3]. Up to date, efforts have been continuously devoted to tailoring acidic properties and improving hydrothermal stability to fulfill the requirement of petrochemical industry. Numerous approaches such as dual-template method [4], post-grafting & crystallization route [5, 6], nanoseed precursors assembly [7–9], fluorocarbon-hydrocarbon surfactants mixture assembly and high-temperature synthesis [10, 11] have been adopted. Comparatively, the strategies of bottom-up and top-down methods [12] are feasible for preparation of mesoporous aluminosilicates with strong acidity and high hydrothermal stability.

A key feature for wide application and design of mesoporous aluminosilicates is the merit of ordered and adjustable mesoporous structure. Transformation from microporous zeolites to mesoporous materials is a milestone [13], which not only extends catalysis and sorption fields, but also improves catalytic and reaction efficiency. Diffusion plays a vital role in heterogeneous catalytic reactions, especially in the reactions with larger guest molecules involved. Based on the recognition of silica materials, relative diffusion performance decreases in the following order: 3D-meso (e.g., SBA-16, 3D-SBA-15) > 1D-meso (e.g., MCM-41) > micro (e.g., microporous zeolites). Though the diffusion of MCM-41 is faster than that of microporous zeolites, MCM-41 still has a relative low diffusion efficiency

Z. Zhang · Z. Yan (✉)  
State Key Laboratory of Heavy Oil Processing, Key Laboratory of Catalysis, CNPC, China University of Petroleum, Qingdao 266555, People's Republic of China  
e-mail: zfyancat@upc.edu.cn

due to the lack of intersected pore system among the adjacent channels, compared with hierarchical and connected mesoporous materials [14]. So it is highly desirable to find a way to improve the connectivity of MCM-41 channels.

SBA-15 [15], MSU-G [16] and SBA-16 [17] materials with interconnected pore system demonstrated unique diffusion performances. The accessibility among pore channels of SBA-15 is manipulated through microspores within the pore walls, the concentration of which is affected by the PEO hydrophilic section of tri-block copolymer and hydrothermal temperature. In addition, MSU-G has poor ordered structures with wormlike channels. Until now, MCF [18], 3D-SBA-15 [19] and polymer microspheres and surfactant co-templated macro/mesoporous monoliths [20] as alternative materials have attracted more attention due to their excellent accessibility between their primary channels. Few studies focused on the development and modification in connectivity of adjacent pores for MCM-41 [21, 22].

Reviewing the literature research, the interconnected channels are also concomitant with the phenomenon of hysteresis loop at high relative pressure (HLHP) of  $N_2$  sorption isotherm, which is dependent on specific MCM-41 synthetic route and usually present in neutralization routes. Initial concept proposed that the hysteresis loop was attributed to interparticular or slitlike pores. Mou first reported the discovery of meso-voids in Al-MCM-41 with tubular morphology, investigated the influence of synthetic factors such as aluminum source,  $H_2O$  and templates on the evolution of meso-voids, and finally made relationships between synthetic conditions and meso-voids [23]. Later, the synthesized Al-MCM-41 showed a superior dehydrogenation and desulfurization performance due to the enhancement of diffusion by auxiliary void defects in catalyst [24, 25]. A similar observation was found in nanocluster self-assembly, it was speculated that void defects were relevant to the additional silica precursors and co-assembly effect [26]. While in Al-MSU-S synthetic conditions, Bagshaw [27] proposed a mechanism that Al enrichment contributed to unsymmetrical formation and intraparticular void defects by correlating intraparticular structure with hysteresis loop. Li [28] and Xiao [29] attributed the formation of void defects to the rigidity of zeolite precursors. In a conventional synthesis, Zhu tuned synthetic conditions including pH values and additives, further revealed Al-MCM-41 with void defects demonstrated a good adsorption capacity of N-nitrosopyrrolidine due to the enhancement of the void defects [30].

It is a cognition and controversial phenomenon regarding HLHP and formation of void defects. In this study, series of mesoporous aluminosilicates (Al-MCM-41) were rationally synthesized by a typical top-down approach, coupling alkali-treatment and self-assembly. It was found

that void defects were relevant to degree of alkali-treatment. A possible mechanism was given out to explain the evolution of void defects.

## 2 Experimental

### 2.1 Preparation of mesoporous aluminosilicates

Mesoporous aluminosilicates Al-MCM-41 (denoted as ZFM) were prepared in a basic and hydrothermal condition, following the procedure reported by Song [31]. In a typical synthesis, 5 g of ZSM-5 was mixed with 100 mL of sodium hydroxide solution (1 mol/L), the obtained suspension was then transferred to three-neck flask and stirred at 353 K in water bath for 1 h. Afterwards, the dissolved solution was instantly cooled down to room temperature followed by filtration. A homogeneous filtrate and 7.5 wt% 60 mL CTAB solution were mixed with stirring for 10 min. The pH value was adjusted to 10.5 with the titration of 2 M  $H_2SO_4$ , finally the gel was transferred to Teflon-lined stainless steel autoclave (150 mL) for crystallization at 383 K for 24 h. The white product was obtained after filtration, drying and calcination in air at 823 K for 6 h. To further investigate the influence of alkali-treatment concentration and stirring time, the prepared sample was coded as ZFM-X-Y h, where X represents alkali-treatment concentration, while Y represents stirring time.

### 2.2 Characterization

X-ray diffraction patterns were recorded on an XPERT-PRO system using  $Cu-K\alpha$  radiation ( $\lambda = 0.154$  nm).  $N_2$  sorption measurements were carried out on Tritstar 3000 apparatus at 77 K. Prior to analysis, the sample was degassed for over 3 h at 573 K under vacuum. Brunauer-Emmett-Teller (BET) method was utilized to calculate the specific surface area at  $P/P_0 = 0.05$ – $0.25$ . The pore size distribution was derived from the desorption branch using the Barrett-Joyner-Halenda (BJH) model, the microporous surface area and microporous volume were calculated from t-plots. Transmission electron microscopy measurements (TEM) were performed on JEM-2100UHR electron microscope. FTIR spectroscopy was recorded on Termo Nicolet Nexus spectrometer with a resolution of  $4\text{ cm}^{-1}$ , using KBr wafer technique. Mercury intrusion porosimetry was carried out on Micromeritics AutoPore IV 9500 apparatus in the range of 0–30,000 psi. The pore diameter was calculated by the equation  $Dp = -\frac{4\delta}{p} \cos \theta$ , assuming a surface tension ( $\delta$ ) of 485 mN/m and contact angle ( $\theta$ ) of  $130^\circ$ .

### 3 Results and discussion

#### 3.1 ZFM mesoporous aluminosilicates

Representative TEM images of ZFM-1.0-1 h are displayed in Fig. 1. It is observed that ZFM-1.0-1 h has well-ordered hexagonal arrays with 1-D channels. Inset in Fig. 1 shows equidistant parallel lines, corresponding to (1 1 0) plane, which are in line with XRD patterns (Fig. 2a). Apart from ordered channels, a large region of brightness (noted by circles) is observed and distributed randomly, which is recognized as void defects [20, 23]. The size of void defects with unique and irregular shape ranges from 5 to 50 nm. It should be noted that void defects are surrounded by short-range ordered channels but with different orientations. Due to the introduction of void defects, the 1D channels are effectively connected [32]. However, the spatial position of void defects [33] should be further investigated with 3-D reconstruction technique [34]. Different architectures surrounding void defects probably result from different favorable growth directions in the nucleation and growth process, and those with different growth directions were not totally perpendicular to the electron beams with somewhat tilts. The developed void

defects render good connectivity and accessibility of ordered channels, accompanied with shortening diffusion path length [35].

In comparison of the samples before and after hydrothermal treatment, the treated samples still preserve well ordered structure, the void defects are not only sporadically distributed in the domain of ordered structure, but still preserve their unique morphology. From the cumulative desorption curves, it is observed that the gap volume, corresponding to the regime with pore size larger than 3 nm, does not change significantly upon hydrothermal treatment. However, the slope of volume versus pore diameter becomes moderate, associated with the disappearance of steep step (Fig. 2d). This phenomenon over ZFM is in line with meso-USY finding showing that vacancies and cavities coalesce to form large mesopores after hydrothermal treatment [33]. It is further certified that the pore system becomes more connective. Textural properties of samples are listed in Table 1.

XRD patterns and  $N_2$  sorption reveal ZFM samples have a high hydrothermal stability. ZFM sample shows four clearly well-resolved peaks that can be indexed as (1 0 0), (1 1 0), (2 0 0) and (2 1 0), associated with the p6 mm hexagonal symmetry with the lattice constant  $a = 44 \text{ \AA}$ . Upon hydrothermal treatment for 4 h at  $600^\circ\text{C}$  in 100 % vapor, three characteristic peaks (1 0 0), (1 1 0) and (2 0 0) could be observed and shift to higher  $2\theta$  degree and the intensity of peaks decreased (Fig. 2a). As displayed in Fig. 2c, hysteresis loop at low relative pressure, corresponding to capillary condensation in primary mesopores, shifts to lower relative pressure after hydrothermal treatment, indicating the shrinkage of pore in the treated sample. Correspondingly, the pore size becomes smaller from  $26 \text{ \AA}$  to  $23 \text{ \AA}$  and pore volume decreases by  $0.24 \text{ cm}^3/\text{g}$ , which evidences the predominant ordered mesopores do not collapse dramatically (Fig. 2d). Interestingly, the microporosity with microporous surface area of  $60.9 \text{ m}^2/\text{g}$  and microporous volume ( $0.02 \text{ cm}^3/\text{g}$ ) vanishes (Fig. 2b). It is speculated that the outstanding hydrothermal stability could be the synergistic results of secondary building units and micropores. Firstly, the introduced secondary building units (5-1 Ring) increase the degree of polymerization, secondly, the silanols (Si–OH) in the existing micropores would further dyhydrolyze into  $\equiv\text{Si–O–Si}\equiv$  bonds, improving the polymerization degree and hydrothermal stability [36].

#### 3.2 Effect of alkali-treatment degree on void defects

##### 3.2.1 Correlation of void defects and pore structure

The results above disclose the formation of void defects in the highly hydrothermal stable Al-MCM-41. To shed light

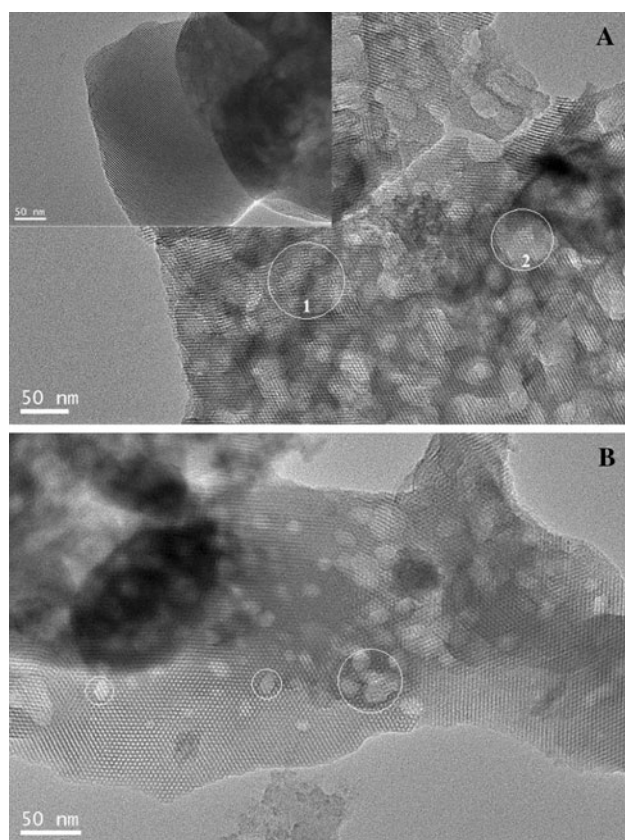


**Fig. 1** TEM images of ZFM-1.0-1 h before (a) and after (b) hydrothermal treatment, Inset is the image taken from the [110] direction

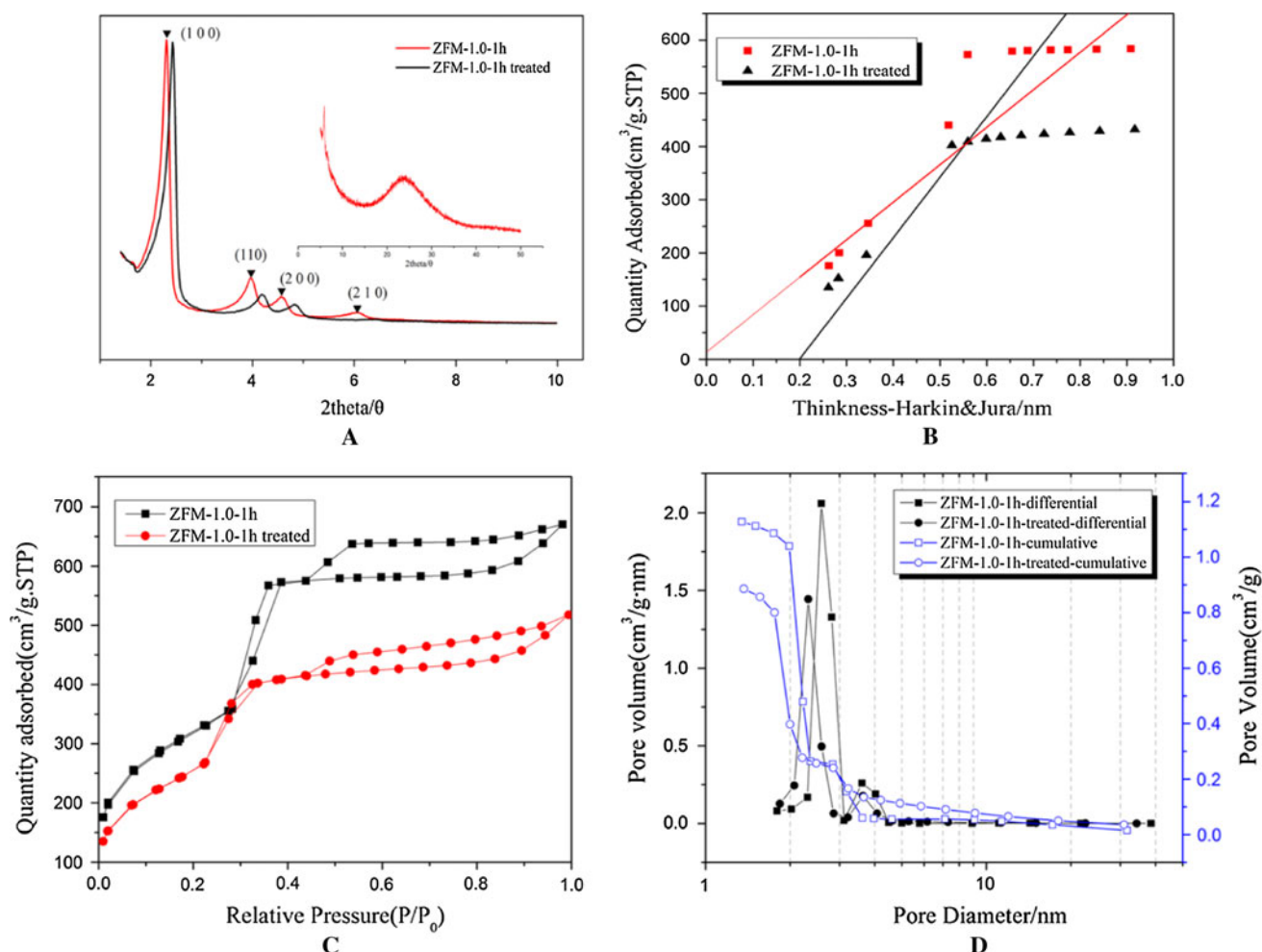


**Fig. 2** **a** XRD patterns of sample ZFM-1.0-1 h before and after hydrothermal treatment, inset is the wide angle of ZFM-1.0-1 h. **b** N<sub>2</sub> sorption isotherms t-plots of ZFM-1.0-1 h before and after hydrothermal

treatment. **c** N<sub>2</sub> adsorption-desorption isotherms of ZFM-1.0-1 h before and after hydrothermal treatment. **d** Pore size distribution and cumulative pore volume curves derived from desorption branch

**Table 1** Textural properties of ZFM-1.0-1 h before and after treatment

Sample	$a_0/\text{\AA}$	$S_{\text{BET}}/\text{m}^2 \text{g}^{-1}$	$V_{\text{total}}/\text{cm}^3 \text{g}^{-1}$	$D_p/\text{\AA}^b$	$D_w/\text{\AA}^c$
ZFM-1.0-1 h	44	1,150	1.04	26	18
ZFM-1.0-1 h-treated <sup>a</sup>	41	1,118	0.80	23	18

<sup>a</sup> Samples was treated in 100 % vapor at 600 °C for 4 h

<sup>b</sup>  $D_p$  was the most probable pore diameter from the desorption isotherm by the BJH model

<sup>c</sup>  $D_w$  (wall thickness) was calculated by the equation:  $D_w = a_0 - D_p$

on the formation and evolution of void defects with alkali-treatment conditions, N<sub>2</sub> sorption and mercury intrusion methods were also employed.

Figure 3a shows N<sub>2</sub> adsorption-desorption isotherms of ZFM-1.0-Yh with different alkali-treatment time. A sharp increase could be observed at relative pressure of 0.2–0.4, corresponding to the capillary condensation [2]. The emergence of hysteresis loop at the above regime implies the connectivity of pore system, because hysteresis loop in

mesoporous solids without interconnected pores is negligible [37]. It is likely that secondary building units incorporated have a significant influence on the wall connectivity. Notably, hysteresis loop at high relative pressure (HLHP) phenomenon is also covered in the isotherms. With the increasing deep recognition and development of characterization technology, HLHP in the MCM-41 materials, could be a reflection of void defects in well-ordered mesoporous materials. Thus, the volume of



HLHP was employed as a tool for semi-quantitative standard of void defects observed in TEM images. The volume of HLHP was evaluated by  $N_2$  adsorbed capacity ( $\text{cm}^3/\text{g.STP}$ ), and  $N_2$  uptake corresponding to the HLHP is defined as the interval from the junction of hysteresis loop to the maximum adsorbed points along the Y axis based on the methodology [23]. Besides, volume adsorbed ( $d > 3.2 \text{ nm}$ ) as a auxiliary standard for void defects is also employed. As shown in Fig. 3a, the volume of HLHP descends with alkali-treatment time increasing, which is similar for volume adsorbed ( $d > 3.2 \text{ nm}$ ). However, the vibration of alkali-treatment time do not significantly affect pore volume and surface area (Table 2). Notably, the pore size distribution and volume fraction are influenced. The total volume is composed of void defects and framework pores. As alkali-treatment time increasing, the corresponding volume of framework increases, while the fraction of void defects decreases (Fig. 3b). In the view of

silicon extraction, prolonged time under the employed alkali-treatment concentration will promote the degradation of dissolved fragments into small pieces such as aluminum tetrahedrons and silicon tetrahedrons, but contributes little to degradation of ZSM-5. Therefore, no significant improvement or decrease on pore structure is observed, which is in agreement with our previous study [38]. It is confirmed that the void defects and large pores diminish with prolonged time.

Apart from the alkali-treatment time, alkali-treatment concentration is another factor influencing the precursors, further affecting the self-assembly. Based on the definition of HLHP, the sorption isotherms of ZFM-X-1 h are displayed in Fig. 3c and corresponding results with respect to volume of HLHP and volume adsorbed ( $d > 3.2 \text{ nm}$ ) are provided in Table 2. As the alkali-treatment concentration arises, the volume adsorbed ( $d > 3.2 \text{ nm}$ ) and volume of hysteresis loop exhibit a decreased trend, when high

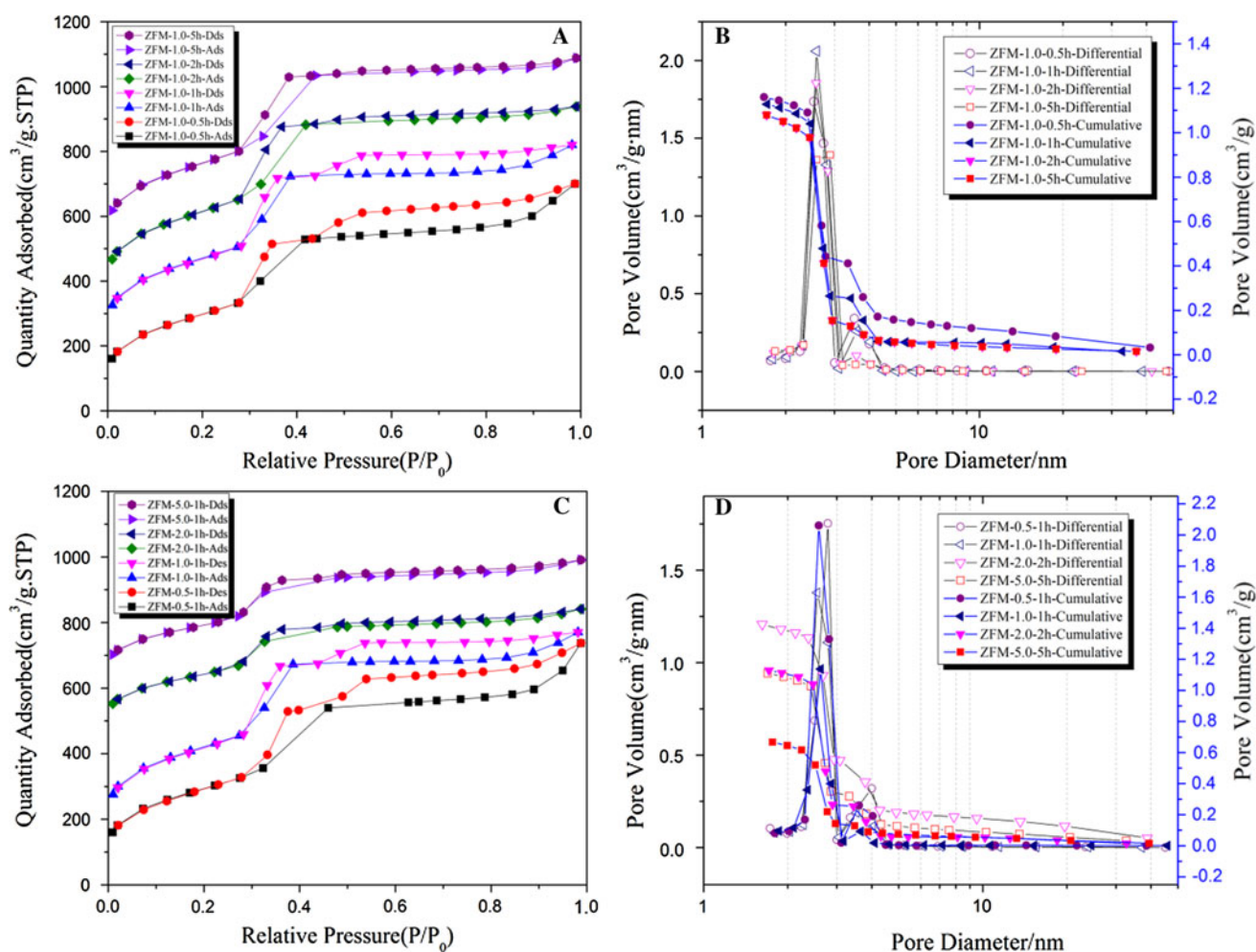


**Fig. 3** **a**  $N_2$  adsorption–desorption isotherms at different alkali-treatment time. The sorption isotherms were offset 0, 150, 300, 450  $\text{cm}^3/\text{g}$ , respectively, for clarity. **b** Pore size distribution and cumulative pore volume curves derived from desorption branch in Fig. 4a. **c**  $N_2$  adsorption–desorption isotherms at different alkali-

treatment concentration. The sorption isotherms were offset 0, 100, 400, 600  $\text{cm}^3/\text{g}$ , respectively, for clarity. **d** Pore size distribution and cumulative pore volume curves derived from desorption branch in Fig. 4c

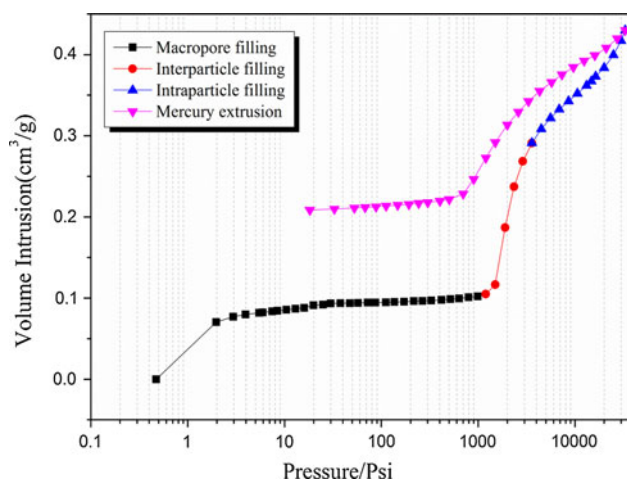
**Table 2** Textural properties of ZFM-X-Y samples

	$S_{\text{BET}}$ ( $\text{m}^2 \text{g}^{-1}$ )	$V_{\text{total}}$ ( $\text{cm}^3 \text{g}^{-1}$ )	$D_p$ ( $\text{\AA}$ )	$V_{(d>3.2 \text{ nm})}$ ( $\text{cm}^3 \text{g}^{-1}$ ) <sup>a</sup>	$V_{\text{HPLP}}$ ( $\text{cm}^3 \text{g}^{-1}$ STP)
ZFM-1.0-0.5 h	1,077	1.08	26	0.413	87
ZFM-1.0-1 h	1,150	1.04	26	0.257	56
ZFM-1.0-2 h	1,143	0.98	26	0.133	12
ZFM-1.0-5 h	1,138	0.98	27	0.130	8
ZFM-0.5-1 h	1,055	1.14	28	0.453	69
ZFM-2.0-1 h	910	0.87	26	0.286	14
ZFM-5.0-1 h	716	0.60	26	0.138	7

<sup>a</sup> Volume adsorbed ( $d > 3.2 \text{ nm}$ ) were calculated from the BJH desorption cumulative pore volume curves

molarities of aqueous NaOH is introduced. Alkali-treatment concentration has a remarkably impact of surface area, pore volume and pore size (Table 2). Because the compositions of ZSM-5 and dissolved solution was strongly affected by the concentration of alkali-treatment, Consequently, the volume of framework pores and void defects both decreased with the increasing alkali-treatment concentration.

Mercury intrusion as a assisted technology is utilized to indentify the intraparticle porosity. Figure 4 shows the function of Hg intrusion volume versus pressure. The intrusion-extrusion curves are comprised by four steps: macropore filling due to powder compression at low pressure ranging from 0 to 1,000 psi, sequential interparticle filling, intraparticle filling at high pressure and mercury extrusion [39]. In the first step of intrusion, the amount of mercury intrusion is due to the powder compression and particle rearrangement with the first knee, the sequential relative broad plateau indicates no further intrusion of Hg in the pressure regime, because the sample was pre-pelleted at 20 Mpa and grounded again. Notably, a distinct mercury increase occurs in the subsequent processes including intreparticle and intraparticle filling.

**Fig. 4** Mercury intrusion-extrusion curves of sample ZFM-1.0-1 h

Mesoporous volume (5–50 nm) derived from the intraparticle filling is  $0.138 \text{ cm}^3/\text{g}$ . Furthermore, a hysteresis phenomenon is also observed at high pressure, indicating an irreversible intrusion-extrusion process. However, the gap between intrusion and extrusion curves is small. Bao [40] reported that the gap could be used as an evaluation criterion of pore connectivity. Therefore, it is revealed that Al-MCM-41 sample has a relative good connectivity in the intraparticle pore structure and void defects including cavities and opening pores are concomitant. 0.2 mL/g of Hg is entrapped in ZFM-1.0-1 h, which is ascribed to the hysteresis and rigidity of compact sample [41].

### 3.2.2 Correlation between void defects and skeleton structure

Coupled with the above characterization results, it is speculated that the quantity of void defects is related to the degree of alkali-treatment. In our previous study [42], the degree of alkali-treatment would affect the quantity of secondary building units and hydrothermal stability. To unveil the relationship between void defects and secondary building units, FTIR spectra of samples varied by the alkali-treatment time are illustrated in Fig. 5. It could be observed that all samples show similar spectrum profiles. ZFM samples exhibit a typical of Al-MCM-41 structure [43]. Bands around  $460 \text{ cm}^{-1}$  are attributed to bending vibration of T-O-T (T = Si or Al), the peaks at 810 and  $1,080 \text{ cm}^{-1}$  are signaled with T-O-T (T = Si or Al) anti-symmetric stretching vibration and symmetric stretching vibration, respectively. In addition, the bands in the region at  $550\text{--}600 \text{ cm}^{-1}$ , which is characteristic of five-membered ring subunits [44], are well-expressed in the spectra of ZFM samples, the results indicate the secondary building units in nanoseed precursors solution were successfully introduced into the pore walls. The intensity of bands at  $550\text{--}600 \text{ cm}^{-1}$  noted with yellow region is varied with alkali-treatment time. As the alkali-treatment time increases, the intensity of bands at  $550\text{--}600 \text{ cm}^{-1}$  reached the maximum with alkali-treatment time of 1 h, indicating that

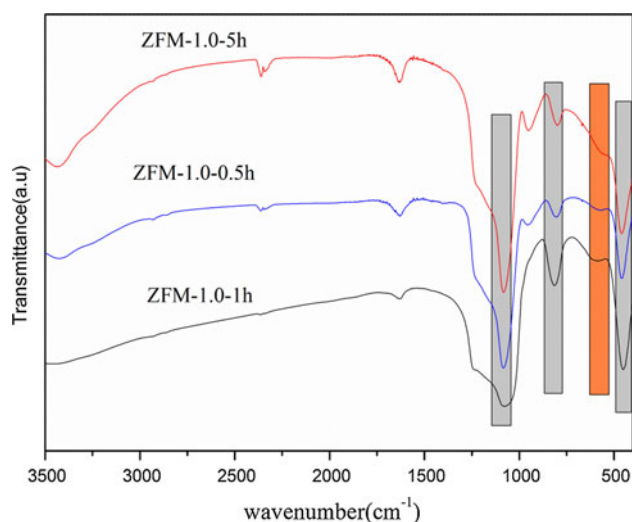


**Fig. 5** FT-IR spectra of as-synthesized samples with different alkali-treatment time

nanoseed precursors undergo the transformation from bulk ZSM-5, 5-membered rings to Si (Al) tetrahedral fundamental units. The species containing 5-membered rings was influenced by the alkali-treatment time, which is in consistent with Inagaki research [45].

### 3.3 Proposed pathways for generation of void defects

In the present work, alkali-treatment concentration and time are tuned to investigate the impact on volume of hysteresis loop at high relative pressure and quantity of void defects. Coupled with FT-IR results, it is considered that the void defects are relevant to the structure of degraded Si (Al) species in the formed gel solution. The

formation mechanism (Fig. 6) of void defects could be tentatively deduced as follows: The synthesis of ZFM is composed of two steps: (1) Alkali-treatment of ZSM-5. (2) Self-assembly of silicon and aluminum precursors on CTAB micelles. In the first step, treated ZSM-5 and dissolved Si (Al) species are obtained by the degradation of ZSM-5 in alkaline solution. The dissolved Si (Al) species, including fragments of secondary building units and isolated Si (Al) tetrahedrons, are the precursors of Al-MCM-41. Furthermore, secondary building units are meta-stable, compared with isolated Si (Al) tetrahedrons. It is reported that the structure of secondary building units is a transit phase for further synthesizing zeolite Y and ZSM-5 [46, 47], and dissolved and isolated Si (Al) tetrahedrons would react with secondary building units due to high reaction activity of SBU structure [48]. To become stable in alkaline solution, secondary building units are inclined to become larger and reach a stable state upon aggregation and reaction with isolated Si (Al) tetrahedrons. The aggregated secondary building units are abbreviated as ASBU. It is concluded that there are different Si (Al) species in the precursor solution, including isolated Si (Al) species, fragments of secondary building units and aggregated secondary building units, and the distribution is dependent on the alkali-treatment condition.

In the sequential step, due to strong interaction of inorganic Si (Al) species and micelle templates, Si (Al) precursors assemble and polymerize on the surface of CTAB micelles, resulting in the formation of hexagonal structure. It is worthy of noting that the size of aggregated secondary building units is larger than the thickness of wall (ca. 2 nm) of MCM-41. Therefore, it is relatively difficult to accommodate the bricks of aggregated building units

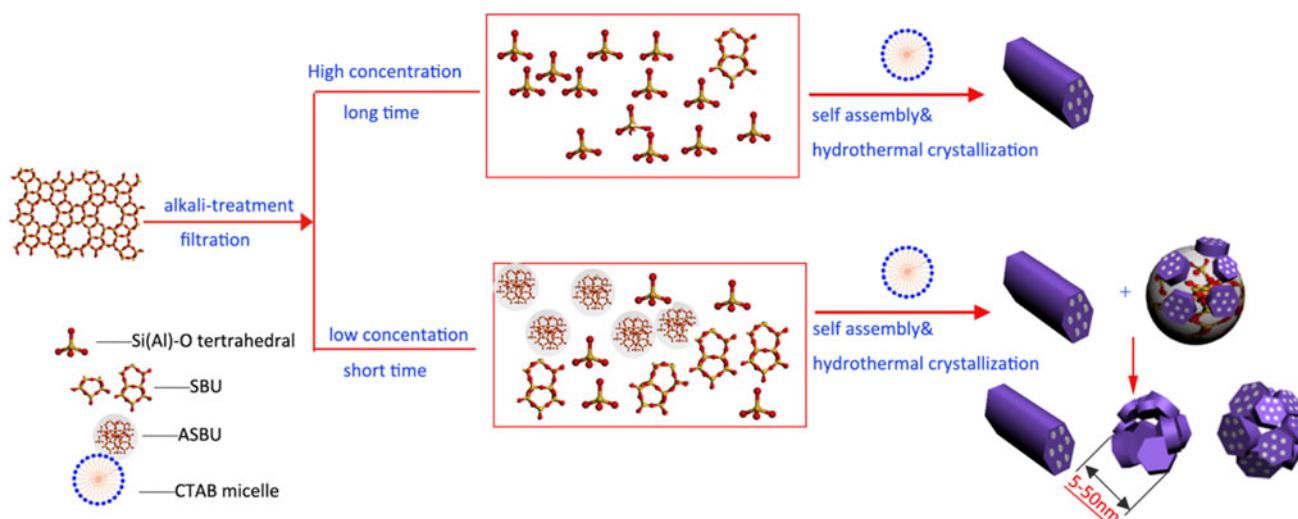


**Fig. 6** Proposed formation mechanism of ZFM sample with void defects

into the mesopore walls as precursors due to the unfavorable spatial restriction [3]. Nucleus center is a necessity for crystal growth. Thus, special aggregated secondary building units dispersed in the solution could act as nuclear centers for further growth. CTAB micelles are electrostatically adsorbed onto exposed surface of aggregated secondary building units, and partial formed meso-structure would also be adsorbed on the ASBU for secondary overgrowth. Concomitant with assembly and growth based on the nucleus of aggregated secondary building units, aggregated secondary building units will gradually dissolve and function as a precursor of Si (Al) species for further formation of meso-structure in the process of sol–gel and hydrothermal crystallization. As shown in Fig. 3, the void defects are affected by the degree of alkali-treatment, because the degree of alkali-treatment will impact the quantity of aggregated secondary building units. High concentration of alkaline and prolonged time both promote the destruction of fragments of SBU structure, inducing the formation of isolated Si (Al) tetrahedrons. Thus, void defects would not be formed in the absence of aggregated secondary building units, which is observed from the negligible volume of hysteresis loop at high pressure in the harsh conditions of alkali-treatment. In the process of nucleation and growth, the most favorable pattern of growth is applied, based on the lowest energy principle. Therefore, different orientations of meso-structure could be observed in the surrounding of void defects.

#### 4 Conclusions

Highly hydrothermally stable Al-MCM-41 was prepared via the top-down strategy coupling degradation and self-assembly. The prepared Al-MCM-41 demonstrated a hierarchical structure including ordered hexagonal channels and void defects (5–50 nm). Furthermore, the void defects as intraparticular porosity were distributed among the ordered meso-structure. The proportion of framework pores and void defects depended on the alkali-treatment conditions of ZSM-5. Severe alkali-treatment conditions induced the extinction of void defects. Even though the void defects were composed of cavities and opening pores, Al-MCM-41 with void defects favors diffusion and mass transportation due to accessibility of adjacent pores in MCM-41 framework pores. Aggregated secondary building units as a sacrificial template contributed to the evolution of void defects. Highly hydrothermally stable Al-MCM-41 with interconnected void defects would be a promising sorbent and catalyst.

**Acknowledgments** Major project funding was provided by the China National Petroleum Company(2010E-1908).

#### References

1. A. Corma, *Chem. Rev.* **97**, 2373 (1997)
2. C.T. Kresge, M.E. Leonowicz, W.J. Roth, J.C. Vartuli, J.S. Beck, *Nature* **359**, 710 (1992)
3. I. Díaz, V. Alfredsson, Y. Sakamoto, *Curr. Opin. Colloid Interface Sci.* **11**, 302 (2006)
4. N. Petkov, M. Hözl, T.H. Metzger, S. Mintova, T. Bein, *J. Phys. Chem. B* **109**, 4485 (2005)
5. Y. Fang, H. Hu, *J. Am. Chem. Soc.* **128**, 10636 (2006)
6. K. Richard Klotz, J. C. Jansen, *Chem. Commun.* 2281 (1997)
7. Y. Liu, W. Zhang, T.J. Pinnavaia, *J. Am. Chem. Soc.* **122**, 8791 (2000)
8. Z. Zhang, Y. Han, F.-S. Xiao, S. Qiu, L. Zhu, R. Wang, Y. Yu, Z. Zhang, B. Zou, Y. Wang, H. Sun, D. Zhao, Y. Wei, *J. Am. Chem. Soc.* **123**, 5014 (2001)
9. Y. Liu, W. Zhang, T.J. Pinnavaia, *Angew. Chem. Int. Ed.* **40**, 1255 (2001)
10. F.-S. Xiao, *Curr. Opin. Colloid Interface Sci.* **10**, 94 (2005)
11. N. Xiao, L. Wang, S. Liu, Y. Zou, C. Wang, Y. Ji, J. Song, F. Li, X. Meng, F.-S. Xiao, *J. Mater. Chem.* **19**, 661 (2009)
12. F.N. Gu, F. Wei, J.Y. Yang, N. Lin, W.G. Lin, Y. Wang, J.H. Zhu, *Chem. Mater.* **22**, 2442 (2010)
13. Y. Tao, H. Kanoh, L. Abrams, K. Kaneko, *Chem. Rev.* **106**, 896 (2006)
14. N. Li, J.-G. Wang, J.-X. Xu, J.-Y. Liu, H.-J. Zhou, P.-C. Sun, T.-H. Chen, *Nanoscale* **4**, 2150 (2012)
15. D. Zhao, J. Feng, Q. Huo, N. Melosh, G.H. Fredrickson, B.F. Chmelka, G.D. Stucky, *Science* **279**, 548 (1998)
16. S.S. Kim, W. Zhang, T.J. Pinnavaia, *Science* **282**, 1302 (1998)
17. Y. Sakamoto, M. Kaneda, O. Terasaki, D.Y. Zhao, J.M. Kim, G. Stucky, H.J. Shin, R. Ryoo, *Nature* **408**, 449 (2000)
18. P. Schmidt-Winkel, W.W. Lukens, D. Zhao, P. Yang, B.F. Chmelka, G.D. Stucky, *J. Am. Chem. Soc.* **121**, 254 (1998)
19. J. Fan, C. Yu, L. Wang, B. Tu, D. Zhao, Y. Sakamoto, O. Terasaki, *J. Am. Chem. Soc.* **123**, 12113 (2001)
20. Z. Sun, Y. Deng, J. Wei, D. Gu, B. Tu, D. Zhao, *Chem. Mater.* **23**, 2176 (2011)
21. M. Kruk, M. Jaroniec, R. Ryoo, S.H. Joo, *J. Phys. Chem. B* **104**, 7960 (2000)
22. B. Coasne, A. Galarneau, F. Di Renzo, R.J.M. Pellenq, *Langmuir* **22**, 11097 (2006)
23. H.-P. Lin, S.-T. Wong, C.-Y. Mou, C.-Y. Tang, *J. Phys. Chem. B* **104**, 8967 (2000)
24. T.-R. Ling, B.-Z. Wan, H.-P. Lin, C.-Y. Mou, *Ind. Eng. Chem. Res.* **48**, 1797 (2009)
25. S.-T. Wong, H.-P. Lin, C.-Y. Mou, *Appl. Catal. A Gen.* **198**, 103 (2000)
26. J. Zheng, S. Zhai, Y. Zhang, D. Wu, Y. Sun, Y. Yang, L. Chen, F. Deng, *Catal. Today* **93–95**, 529 (2004)
27. S.A. Bagshaw, S. Jaenicke, C.G. Khuan, *Ind. Eng. Chem. Res.* **42**, 3989 (2003)
28. Y. Li, J. Shi, H. Chen, Z. Hua, L. Zhang, M. Ruan, J. Yan, D. Yan, *Micropor. Mesopor. Mater.* **60**, 51 (2003)
29. D. Li, D.S. Su, J. Song, X. Guan, K. Hofmann, F.-S. Xiao, *J. Mater. Chem.* **15**, 5063 (2005)
30. F. Gu, J. Yang, F. Wei, J. Zhu, *Chin. J. Catal.* **31**, 267 (2010)
31. C.-M. Song, J. Jiang, Z.-f. Yan et al., *J. Porous Mater.* **15**, 205 (2008)
32. J. Liu, J. Yang, Q. Yang, G. Wang, Y. Li, *Adv. Funct. Mater.* **15**, 1297 (2005)
33. A.H. Janssen, A.J. Koster, K.P. de Jong, *J. Phys. Chem. B* **106**, 11905 (2002)
34. K.P. de Jong, A.J. Koster, *ChemPhysChem* **3**, 776 (2002)



35. M. Choi, K. Na, J. Kim, Y. Sakamoto, O. Terasaki, R. Ryoo, *Nature* **461**, 246 (2009)
36. F. Zhang, Y. Yan, H. Yang, Y. Meng, C. Yu, B. Tu, D. Zhao, *J. Phys. Chem. B* **109**, 8723 (2005)
37. K.L. Murray, N.A. Seaton, M.A. Day, *Langmuir* **15**, 8155 (1999)
38. Z. Zhang, J. Xiao, L. Dai, Y. Wang, D. Wang, X. Liu, Z. Yan, *J. Porous Mater.* (2011). doi:[10.1007/s10934-011-9496-3](https://doi.org/10.1007/s10934-011-9496-3)
39. J. Rouquerol, G.V. Baron, R. Denoyel, H. Giesche, J. Groen, P. Klobes, P. Levitz, A.V. Neimark, S. Rigby, R. Skudas, K. Sing, M. Thommes, K. Unger, *Micropor. Mesopor. Mater.* **154**, 2 (2012)
40. Q. Tan, X. Bao, T. Song, Y. Fan, G. Shi, B. Shen, C. Liu, X. Gao, *J. Catal.* **251**, 69 (2007)
41. J.C. Groen, W. Zhu, S. Brouwer, S.J. Huynink, F. Kapteijn, J.A. Moulijn, J. Perez-Ramirez, *J. Am. Chem. Soc.* **129**, 355 (2006)
42. C.M. Song, *Synthesis, Characterization and Application of Micro-Mesoporous Composite Aluminosilicate Molecular Sieves*. China University of Petroleum, 2006
43. M. Adjdir, T. Ali-Dahmane, P.G. Weidler, C. R. Chim. **12**, 793
44. C.E.A. Kirschhock, R. Ravishankar, F. Verspeurt, P.J. Grobet, P.A. Jacobs, J.A. Martens, *J. Phys. Chem. B* **103**, 4965 (1999)
45. S. Inagaki, M. Ogura, T. Inami, Y. Sasaki, E. Kikuchi, M. Matsukata, *Micropor. Mesopor. Mater.* **74**, 163 (2004)
46. R. Xu, W. Pang, J. Yu, Q. Huo, J. Chen, *Chemistry of Zeolites and Porous Materials* (Scientific Press, Beijing, 2004), p. 39
47. F. Ocampo, H.S. Yun, M.M. Pereira, J.P. Tessonier, B. Louis, *Cryst. Growth Des.* **9**, 3721 (2009)
48. A. Čimek, B. Subotić, I. Šmit, A. Tonejc, R. Aiello, F. Crea, A. Nastro, *Micropor. Mater.* **8**, 159 (1997)